

ARTICLE

DOI: 10.1038/s41467-018-05272-8

OPEN

Probing the coordination and function of Fe_4S_4 modules in nitrogenase assembly protein NifB

Lee A. Rettberg¹, Jarett Wilcoxon², Chi Chung Lee¹, Martin T. Stiebritz¹, Kazuki Tanifuji¹, R. David Britt² & Yilin Hu¹

NifB is an essential radical *S*-adenosylmethionine (SAM) enzyme for nitrogenase cofactor assembly. Previous studies show that NifB couples a putative pair of $[\text{Fe}_4\text{S}_4]$ modules (designated K1 and K2) into an $[\text{Fe}_8\text{S}_9\text{C}]$ cofactor precursor concomitant with radical SAM-dependent carbide insertion through the action of its SAM-binding $[\text{Fe}_4\text{S}_4]$ module. However, the coordination and function of the NifB cluster modules remain unknown. Here, we use continuous wave and pulse electron paramagnetic resonance spectroscopy to show that K1- and K2-modules are 3-cysteine-coordinated $[\text{Fe}_4\text{S}_4]$ clusters, with a histidine-derived nitrogen serving as the fourth ligand to K1 that is lost upon K1/K2-coupling. Further, we demonstrate that coexistence of SAM/K2-modules is a prerequisite for methyltransfer to K2 and hydrogen abstraction from the K2-associated methyl by a 5'-deoxyadenosyl radical. These results establish an important framework for mechanistic explorations of NifB while highlighting the utility of a synthetic-cluster-based reconstitution approach employed herein in functional analyses of iron-sulfur (FeS) enzymes.

¹Department of Molecular Biology and Biochemistry, University of California, Irvine, CA 92697-3900, USA. ²Department of Chemistry, University of California, Davis, CA 95616, USA. These authors contributed equally: Lee A. Rettberg, Jarett Wilcoxon. Correspondence and requests for materials should be addressed to R.D.B. (email: rdbritt@ucdavis.edu) or to Y.H. (email: yilinh@uci.edu)

Nitrogenase is a complex metalloenzyme that catalyzes the remarkable chemical transformations of N_2 to NH_3 , and CO to hydrocarbons, at its cofactor site^{1–5}. Designated the M-cluster, the cofactor of the Mo-nitrogenase is a [MoFe₇S₉C(R-homocitrate)] cluster comprising [MoFe₃S₃] and [Fe₄S₃] sub-clusters ligated by three μ_2 -sulfides and one μ_6 -interstitial carbide, with an R-homocitrate moiety providing further coordination to its terminal Mo atom^{6–8}. The unique reactivity of M-cluster has sparked interest in elucidating its biosynthetic mechanism. Such knowledge is crucial for understanding the structure–function relationship of nitrogenase, which in turn could facilitate future development of biomimetic catalysts for ambient conversion of N_2 and C_1 substrates into valuable chemical commodities. Previous studies have led to the proposal of a working model of M-cluster assembly (Supplementary Fig. 1)^{9–20}. The early stage of this process involves the coupling and rearrangement of two putative [Fe₄S₄] clusters (designated the K-cluster) on an assembly scaffold, NifB, concomitant with the insertion of an interstitial carbide and a 9th sulfur, giving rise to a [Fe₈S₉C] core (designated the L-cluster) that is nearly indistinguishable in structure from the M-cluster (Supplementary Fig. 1a, i–iii). Subsequently, the 8Fe L-cluster is matured into an M-cluster on another assembly scaffold, NifEN, upon substitution of a Mo-homocitrate conjugate for one terminal Fe atom of the cluster by NifH, the cofactor maturase (Supplementary Fig. 1a, iv). Finally, the M-cluster is transferred to its target binding site in NifDK, the catalytic component of Mo-nitrogenase (Supplementary Fig. 1a, v).

Of all components along the M-cluster assembly pathway, NifB plays a pivotal role in transforming small, putative 4Fe units (K-cluster) into an 8Fe entity (L-cluster) that has the complete FeS core structure in place, as well as the interstitial carbide. A member of the radical S-adenosyl-L-methionine (SAM) enzyme family^{21,22}, NifB carries the signature CxxxCxxC radical SAM motif, as well as a number of ligands that could accommodate coordination of the entire complement of Fe atoms of the M-cluster^{9,10,23}. Characterization of the NifB proteins from *Azotobacter vinelandii*^{11–13} and *Methanosarcina acetivorans*¹⁴ has unveiled a radical SAM-dependent mechanism employed by NifB for carbide insertion, which begins with methyltransfer in an S_N2 -type mechanism from SAM to a putative [Fe₄S₄] cluster pair (Supplementary Fig. 1b, i). Subsequently, the transferred methyl group undergoes hydrogen abstraction by a SAM-derived 5'-deoxyadenosyl (5'-dA•) radical (Supplementary Fig. 1b, ii). This step is followed by further deprotonation and/or dehydrogenation of the resultant carbon radical, which occurs concomitantly with the coupling and rearrangement of the putative [Fe₄S₄] clusters pair into an [Fe₈S₉C] core via radical chemistry (Supplementary Fig. 1b, iii). Together, these results suggest the presence and concerted action of three 4Fe modules, namely, the two 4Fe modules (designated the K1- and K2-modules) that give rise to the K-cluster and a third 4Fe module that is ligated by the radical SAM motif (designated the SAM-module), on NifB. However, despite the past and recent progress toward elucidating the NifB-catalyzed reaction^{11–14,23–27}, questions remain open as to the 4Fe nature of the building blocks used to generate the 8Fe core, the coordination of the different cluster modules in NifB, and the biosynthetic event that occurs on each of these NifB-associated cluster modules.

Here, we show that NifB variants carrying the individual K1-, K2- and SAM-modules can be reconstituted with synthetic [Fe₄S₄] clusters, thereby providing conclusive evidence that NifB consists of three distinct 4Fe modules. Continuous wave (CW)- and pulse EPR analyses reveal that both K1- and K2-modules are coordinated by 3 Cys ligands, with a His residue providing an additional nitrogen ligand to the K1 module that is lost upon coupling of the K1- and K2-modules into an 8Fe

core; whereas biochemical experiments further demonstrate that coexistence of the SAM- and K2-modules is a prerequisite for methyltransfer to the K2-derived sulfide atom and the subsequent hydrogen abstraction from the K2-associated methyl group by a 5'-dA• radical. These results not only lay an important foundation for further mechanistic investigations of the NifB-catalyzed reactions, but also point to the utility of the synthetic-cluster-based reconstitution protocol in functional analyses of other FeS systems.

Results

Establishing the 4Fe nature of the NifB-associated clusters. A series of variants—each carrying one of the three proposed 4Fe modules—was generated on the template of the NifB protein from *M. acetivorans* (designated *MaNifB*). Previously, *MaNifB* was successfully expressed in *Escherichia coli*¹⁴. Sequence analysis of *MaNifB* reveals the presence of three groups of highly conserved Cys residues—three Cys residues per group—that could potentially serve as ligands for the SAM-, K1-, and K2-modules of NifB (Fig. 1a, b). Specifically, Cys⁵⁰, Cys⁵⁴, and Cys⁵⁷, which form the canonical CxxxCxxC radical SAM motif, are assigned to the SAM-module; Cys³⁰, Cys⁶³, and Cys¹²⁹, which are located toward the N terminus of the primary sequence, are assigned to the K1 module; and Cys²⁶⁴, Cys²⁷⁴, and Cys²⁷⁷, which are positioned toward the C terminus of the primary sequence, are assigned to the K2 module (Fig. 1a, b). On the basis of the tentative assignment of the Cys residues, each cluster-binding module of *MaNifB* can be studied independently by mutating the Cys ligands of the other two modules to Ala. Using this approach, we generated three constructs, each encoding a *MaNifB* variant with a single SAM (designated *MaNifB*^{SAM}), K1 (designated *MaNifB*^{K1}), or K2 (designated *MaNifB*^{K2})-module (see Supplementary Fig. 2, i–iii). We then co-expressed each *MaNifB* variant with the FeS-assembly machinery, IscSUA, in *E. coli*. Purified *MaNifB* variants, like their native counterpart, showed a monomeric composition comprising a 38 kDa subunit (Supplementary Fig. 3). However, the cluster contents of the as-purified *MaNifB* proteins were insufficient for spectroscopic and biochemical analyses. To circumvent this problem, we used a recently developed protocol²⁸ to first remove the endogenous FeS clusters of the *MaNifB* variants and then reconstitute these proteins with a synthetic [Fe₄S₄] compound (see Supplementary Fig. 2). Such a reconstitution approach has been successfully applied to identify the source of the 9th sulfur during the cofactor maturation process on *MaNifB*²⁸ without interference of the Fe/S impurities often introduced by the traditional FeCl₃/Na₂S-based reconstitution method and, in this particular case, it can be used to conclusively determine the [Fe₄S₄] identity of the individual modules in *MaNifB*. Indeed, upon in vitro reconstitution with this synthetic [Fe₄S₄] compound, each of the three *MaNifB* variants has an $S = 1/2$ electron paramagnetic resonance (EPR) signal that is characteristic of a [Fe₄S₄]⁺ cluster when the protein is reduced by dithionite (Fig. 1c; also see Supplementary Table 1 for Fe contents, spin concentrations and protein concentrations of EPR samples). Consistent with their different origins, the simulated spectra have distinct g values from one another (*MaNifB*^{SAM}: $g = [2.017\ 1.924\ 1.910]$; *MaNifB*^{K1}: $g = [2.050\ 1.905\ 1.900]$; *MaNifB*^{K2}: $g = [2.044\ 1.933\ 1.886]$; also see Supplementary Fig. 4 and Supplementary Table 2 for simulation parameters), and the contributions of most EPR features of the individual modules can be identified in the spectrum of the wild-type *MaNifB* (Fig. 1c). These observations are exciting, as they provide strong support for the assignment of the respective Cys residues as the ligands of the three modules in *MaNifB* while supplying direct proof for the [Fe₄S₄] identity of the K1- and K2-modules.

Probing the ligation patterns of NifB-associated clusters. The ligation patterns of the K1- and K2-modules were further explored by pulse EPR spectroscopy, using the one-dimensional electron spin echo envelope modulation (ESEEM) and two-dimensional hyperfine sub-level correlation (HYSCORE) pulse EPR techniques. In particular, we examined the presence of nitrogen coupling—previously reported for a NifB homolog from a different methanogenic organism²⁷—in *MaNifB*^{K1} and *MaNifB*^{K2} in order to assign the nitrogen ligand to a specific cluster module. Interestingly, the three-pulse ESEEM data of *MaNifB*^{wt} and *MaNifB*^{K1} reveal modulations of a nitrogen coupled to the K1-cluster (Fig. 2a, blue trace). Data collected across the EPR absorption envelope of *MaNifB*^{K1} (Supplementary Fig. 5), from $g = 2.050$ to $g = 1.900$, show complex and overlapping peaks from a ¹⁴N nucleus. While these data are rich in information, extracting that information is difficult given the overlap between peaks. In order to further separate out the observed peaks and reliably interpret the ¹⁴N hyperfine and quadrupole couplings, we collected HYSCORE spectra at each of the principal g values for the K1 module. The experimental data are simulated exceedingly well with a ¹⁴N hyperfine coupling tensor (in MHz) of $\mathbf{A} = [2.9 \ 2.9 \ 5.6]$ and a nuclear quadrupole coupling

of $e^2Qq/h = -2.1$ MHz and $\eta = 0.4$ (Fig. 2b, c; also see Supplementary Table 3). The overall hyperfine coupling tensor, \mathbf{A} , can be analyzed as two major components, where $\mathbf{A} = \mathbf{A}_{\text{iso}} + \mathbf{A}_{\text{dip}}$. The first term (\mathbf{A}_{iso}) is the isotropic Fermi contact term, where $\mathbf{A}_{\text{iso}} = (\mathbf{A}_1 + \mathbf{A}_2 + \mathbf{A}_3)/3$; and the second term (\mathbf{A}_{dip}) is the through space dipolar coupling tensor, where $\mathbf{A}_{\text{dip}} = [-T \ -T \ 2T]$. We then compared known values of various N ligands to metal centers (Supplementary Table 3) with the HYSCORE simulation parameters. For a nitrogen directly coordinated to a FeS cluster, an isotropic hyperfine of $\mathbf{A}_{\text{iso}} = 3\text{--}7$ MHz and a dipolar coupling of $T = 0.9\text{--}1$ MHz are expected, while a nitrogen which is near but not coordinated to the cluster, such as a backbone amide, would have an $\mathbf{A}_{\text{iso}} \sim 1$ MHz. Our data suggest the nitrogen we measured ($\mathbf{A}_{\text{iso}}^{\text{K1}} = 3.8$ MHz, $T^{\text{K1}} = 0.9$ MHz) is in fact directly coordinated to the K1 module^{29–39}. Next, we compared the nuclear quadrupole coupling (e^2Qq/h) values of ¹⁴N nuclei, which report on the electric field gradient of the ¹⁴N nucleus and are sensitive to the environment of the nitrogen that is directly bound to an Fe center. While there are numerous EPR measured hyperfine and quadrupole couplings from nitrogenous ligands to Fe sites, a majority of them are from histidine ligated sites, including those found in the various Rieske-type [Fe₂S₂]

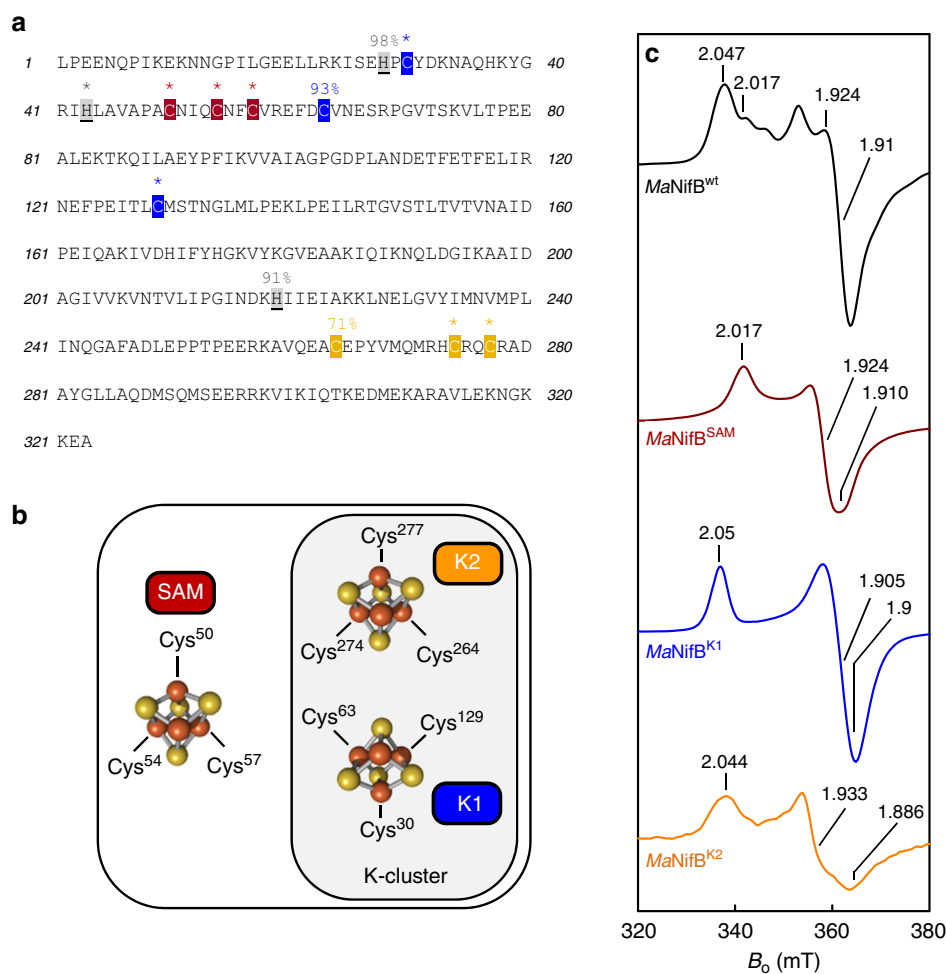


Fig. 1 Assignment of three [Fe₄S₄] cluster modules in *MaNifB*. **a** The primary sequence of *MaNifB*. The Cys and His residues that are conserved among 45 NifB sequences from various organisms¹⁴ are highlighted, with those 100% conserved indicated with a *, and others noted for the percentages of conservation among these organisms. **b** Schematic presentations of the SAM-, K1-, and K2-modules in *MaNifB*. A 3-Cys ligation pattern is proposed for all three modules, with the proposed ligands indicated in each module. **c** EPR spectra of the synthetic [Fe₄S₄] cluster-reconstituted wild-type *MaNifB* (*MaNifB*^{wt}, black) and *MaNifB* variants carrying the SAM (*MaNifB*^{SAM}, brown), K1 (*MaNifB*^{K1}, blue), and K2 (*MaNifB*^{K2}, orange) modules, respectively. The spectra were collected as described in Methods, and the g values of each spectrum are indicated. The CW EPR experiment was performed four times. Representative results are shown in c. See Supplementary Table 1 for Fe contents, spin concentrations and protein concentrations of EPR samples

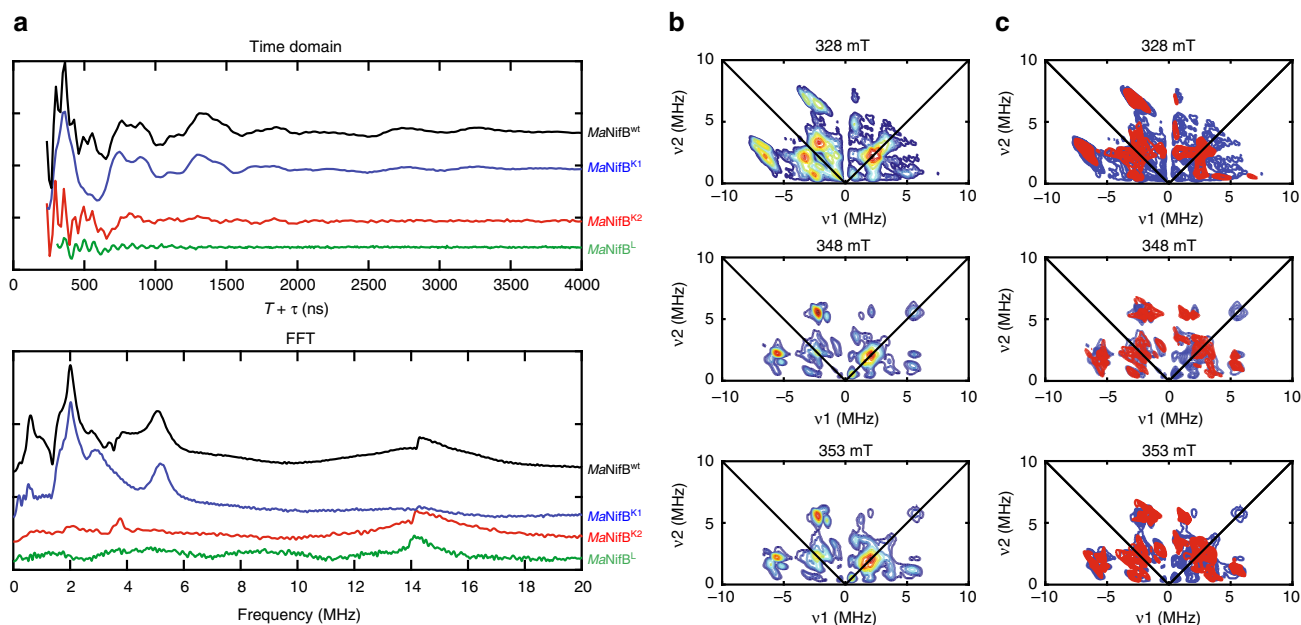


Fig. 2 Pulse EPR analysis of *MaNifB*. **a** Three-pulse ESEEM spectra of dithionite-reduced *MaNifB*^{wt} (black), *MaNifB*^{K1} (blue), *MaNifB*^{K2} (red), and *MaNifB*^L (green). The time domain spectra of *MaNifB*^{wt} and *MaNifB*^{K1} have modulations from ¹⁴N that appear as peaks in the fast Fourier transformed (FFT) spectra between 1 and 8 MHz. The sharp modulations between 250 and 500 ns in the time domain and the resulting broad peak near 14 MHz in the FFT are from nearby weakly coupled protons. **b** HYSCORE spectra of the dithionite-reduced *MaNifB*^{K1} taken at 328, 348, and 353 mT. **c** The HYSCORE data (blue) can be simulated (red) with a single ¹⁴N nucleus, with a hyperfine coupling tensor **A** (in MHz) = [2.9 2.9 5.6] and a quadrupole coupling of $e^2Qq/h = -2.1$ MHz and $\eta = 0.4$. Three-pulse ESEEM spectra were recorded at 10 K, $\tau = 128$ –144 ns (values chosen to minimize proton modulations to the spectra), $\pi/2 = 12$ ns, and a microwave frequency of 9.3366 GHz (*MaNifB*^{wt}, *MaNifB*^{K1}, *MaNifB*^{K2}) or 9.2465 GHz (*MaNifB*^L). Spectra were collected near the g_2 value (spectra maxima) for each of the samples (*MaNifB*^{wt}: 343 mT; *MaNifB*^{K1}: 343 mT, and *MaNifB*^{K2}: 344 mT, and *MaNifB*^L: 340 mT). *MaNifB*^{K1} HYSCORE spectra were recorded at 10 K, $\tau = 128$ –132 ns, and $\pi/2 = 12$ ns

clusters ($e^2Qq/h = 1.9$ – 3.5 MHz) where the cluster contains two His ligands, in the mitoNEET [Fe_2S_2] clusters ($e^2Qq/h = -2.47$ MHz) which contain only a single His ligand, and in myoglobin ($e^2Qq/h = -2.24$ MHz) where the His ligand is axial to the porphyrin-bound Fe center^{30–38,40,41}. The only reported hyperfine and quadrupole coupling from a non-histidine ligand is found in the radical SAM enzyme BioB, where Arg²⁶⁰ is coordinated to a [Fe_2S_2] cluster ($e^2Qq/h = 2.6$ – 2.8 MHz)²⁹. The quadrupole coupling we measured ($e^2Qq/h = -2.1$ MHz) is lower than the reported value for Arg and is in the range of values for a His coordinated cluster; therefore, we assigned the fourth ligand to the K1 module as histidine. Contrary to what we observed in the case of the K1-cluster, we did not detect ¹⁴N coupling to the K2-cluster (in *MaNifB*^{K2}) and the L-cluster (in *MaNifB*^L, or SAM-treated *MaNifB*^{wt}, wherein the K1- and K2-modules are fused into an 8Fe L-cluster upon addition of SAM) by the same EPR techniques (Fig. 2a, red and green traces). However, the observed absence of nitrogen coupling to the K2 module cannot be used to determine if the fourth Fe site of this cluster is open, is occupied by a coordinated water, or is ligated by an amino acid such as Asp or Glu. The absence of nitrogen ligation to the L-cluster, on the other hand, is particularly interesting, as it suggests a conformational rearrangement upon coupling of the K1- and K2-modules into an 8Fe L-cluster.

Defining the functions of NifB-associated modules. Having established the presence of three distinct [Fe_4S_4] modules in *MaNifB*, we set out to address the question of which biosynthetic event occurs on each module and, particularly, how the SAM-module—the place where radical SAM chemistry takes place—works with the K1- and K2-modules during the cluster maturation process. Using our modular approach, two additional

MaNifB variants (see Supplementary Fig. 2, iv, v), one carrying the SAM- and K1-modules (designated *MaNifB*^{SAM+K1}) and the other carrying the SAM- and K2-modules (designated *MaNifB*^{SAM+K2}), were expressed in *E. coli*, followed by purification and reconstitution with the synthetic [Fe_4S_4] compound. Interestingly, the spectrum of neither *MaNifB*^{SAM+K1} nor *MaNifB*^{SAM+K2} is a simple add-up of the individual spectra of the respective cluster modules: the *MaNifB*^{SAM+K2} spectrum resembles the *MaNifB*^{SAM} spectrum in line-shape, but is somewhat broadened and displayed a new $g_{\text{app}} = 1.92$ feature (Fig. 3a, green trace); whereas the *MaNifB*^{SAM+K1} spectrum resembles the *MaNifB*^{K1} spectrum in line-shape, but is clearly broadened and displays a distinct $g_{\text{app}} = 1.95$ feature in addition (Fig. 3a, blue trace). HPLC analysis further reveals that, like the wild-type *MaNifB*, *MaNifB*^{SAM+K2} is capable of cleaving SAM into *S*-adenosyl-L-homocysteine (SAH) and 5'-deoxyadenosine (5'-dAH); in contrast, *MaNifB*^{SAM+K1}, along with *MaNifB*^{SAM}, *MaNifB*^{K1}, and *MaNifB*^{K2}, is unable to generate SAH or 5'-dAH upon incubation with SAM (Fig. 3b, c). This observation suggests that the presence of both SAM- and K2-modules is the prerequisite for both SAM-related reactions to occur during the cluster maturation process, with the K2 module serving as the final location for methyl attachment and the SAM-module supplying a 5'-dA• radical for hydrogen abstraction of the K2-associated methyl group. Consistent with this suggestion, the formation of methanethiol is only detected upon acid quench of an incubation mixture of *MaNifB*^{SAM+K2} and SAM, pointing to the attachment of SAM-derived methyl group to a sulfide of the K2 module (Fig. 3d).

Discussion

A refined pathway of the K- to L-cluster conversion on NifB (Fig. 4) can be proposed based on these results, as well as those

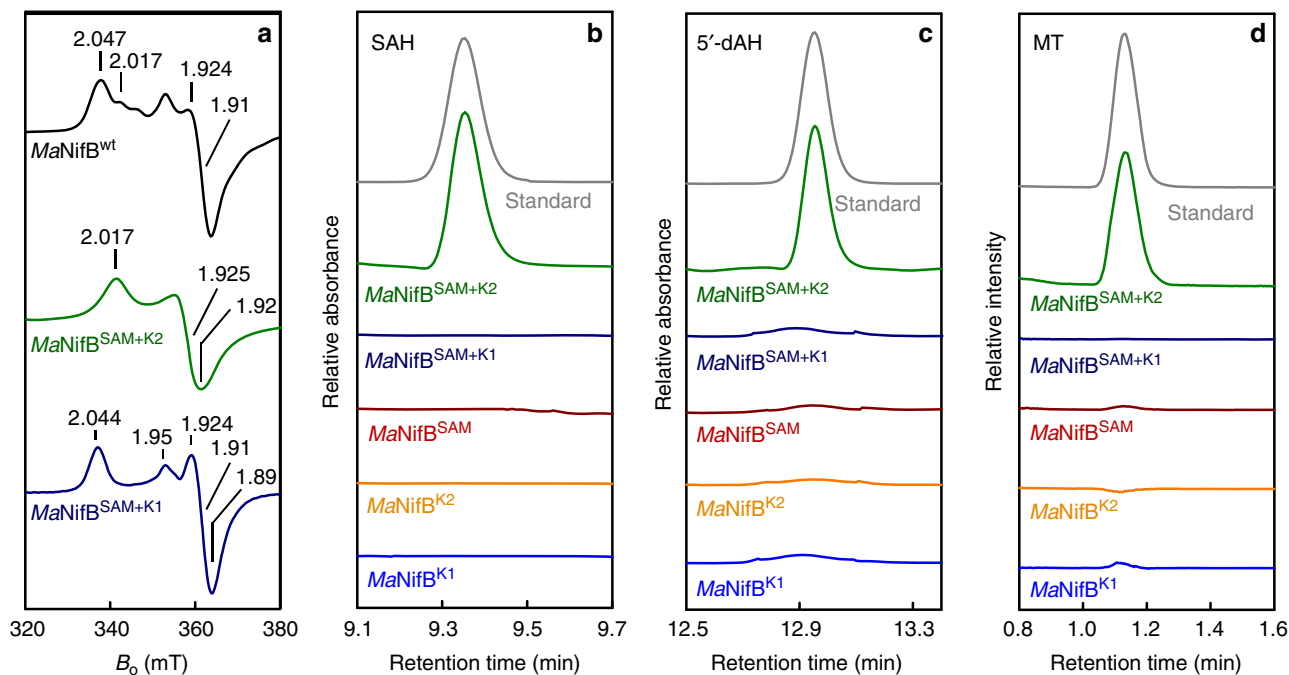


Fig. 3 Spectroscopic and functional properties of the cluster modules in *MaNifB*. **a** EPR spectra of the synthetic $[\text{Fe}_4\text{S}_4]$ cluster-reconstituted wild-type *MaNifB* ($\text{MaNifB}^{\text{wt}}$, black) and *MaNifB* variants carrying SAM plus K2 ($\text{MaNifB}^{\text{SAM+K2}}$, green) and SAM plus K1 ($\text{MaNifB}^{\text{SAM+K1}}$, dark blue) modules, respectively. **b, c** HPLC elution profiles of SAH (**b**) and 5'-dAH (**c**) standards (gray), and those of SAM incubated with *MaNifB* variants carrying K1 ($\text{MaNifB}^{\text{K1}}$, light blue), K2 ($\text{MaNifB}^{\text{K2}}$, orange), SAM ($\text{MaNifB}^{\text{SAM}}$, brown), SAM plus K1 ($\text{MaNifB}^{\text{SAM+K1}}$, dark blue), and SAM plus K2 ($\text{MaNifB}^{\text{SAM+K2}}$, green) modules, respectively. **d** GC analyses of the methanethiol (MT) standard (gray) and acid-quenched incubation mixtures containing SAM and *MaNifB* variants carrying K1 ($\text{MaNifB}^{\text{K1}}$, light blue) and K2 ($\text{MaNifB}^{\text{K2}}$, orange), SAM ($\text{MaNifB}^{\text{SAM}}$, brown), SAM plus K1 ($\text{MaNifB}^{\text{SAM+K1}}$, dark blue), and SAM plus K2 ($\text{MaNifB}^{\text{SAM+K2}}$, green) modules, respectively. The CW EPR (**a**), HPLC (**b, c**), and GC (**d**) experiments were performed three times each. Representative results are shown in the figure. See Supplementary Table 1 for Fe contents and protein concentrations of EPR samples

from a recent work that traced the origin and insertion of the 9th sulfur of the cofactor²⁸. This pathway starts with methyltransfer from one equivalent of SAM to a bridging sulfide of the K2 module via an $\text{S}_{\text{N}}2$ -type mechanism, followed by generation of a 5'-dA• radical via homolytic cleavage of a second equivalent of SAM bound to the SAM-module, and abstraction of a hydrogen atom from the K2-bound methyl group. These events result in a K2-bound methylene ($-\text{CH}_2\bullet$) radical, which then initiates the coupling/rearrangement of the K2- and K1-modules into an L^{*}-cluster ($[\text{Fe}_8\text{S}_8\text{C}]$) that has the core structure of the L-cluster ($[\text{Fe}_8\text{S}_9\text{C}]$) except for the absence of the 9th sulfur in the belt region of the cluster. Subsequently, the 9th sulfur is inserted concomitantly with further dehydrogenation or deprotonation of the carbon intermediate until a μ_6 -coordinated C^{4-} ion appears in the central cavity of the cluster. Of the various reactions catalyzed by NifB, the $\text{S}_{\text{N}}2$ -type methyltransfer and the subsequent hydrogen abstraction from the methyl are similar to the reactions catalyzed by Cfr and RlmN, two radical SAM enzymes involved in the methylation of rRNA^{42–44}.

The cluster transformation process requires structural rearrangement to allow the formation of an L-cluster and the subsequent transfer of the L-cluster from NifB onto the next biosynthetic apparatus, NifEN, along the cofactor assembly pathway (Fig. 4). Central to the structural rearrangement is the loss of the N ligand to the K1 module, as well as possible loss of additional Cys ligands to the K1- and K2-modules. This type of labile N ligand is also observed in mitoNEET, where a single His coordination to a $[\text{Fe}_2\text{S}_2]$ cluster is involved in the release of the cluster to downstream acceptor proteins through a protonation event^{45,46}. It is important to note the complexity of the reaction catalyzed by NifB, where there are two substrate molecules of SAM, two substrate $[\text{Fe}_4\text{S}_4]$ clusters (i.e., K1- and K2-clusters),

and a catalytic $[\text{Fe}_4\text{S}_4]$ cluster (i.e., the SAM-cluster). These $[\text{Fe}_4\text{S}_4]$ clusters can be sensitive to degradation, especially when there is a non Cys-ligated, open Fe site. Therefore, it is advantageous to have a ligand (like the histidine ligand for the K1-cluster) which, triggered by protonation, can be released from the $[\text{Fe}_4\text{S}_4]$ cluster module to facilitate the formation of the much more stable $[\text{Fe}_8\text{S}_9\text{C}]$ L-cluster.

Another interesting point to note is the absence of 5'-dAH formation in the sole presence of the SAM-module, and the absence of SAH formation in the sole presence of the K2 module. While the former could be explained by a lack of K2-bound methyl group that can undergo hydrogen atom abstraction by a 5'-dA• radical, the latter could be accounted for by the absence of a nearby SAM-module that renders the K2-cluster in the correct oxidation state for methyl attachment. A previous study has shown that methyltransfer does not occur when NifB is oxidized or reduced by a weak reductant, suggesting that the K-cluster needs to be poised in a certain redox state to render its associated sulfides more nucleophilic for methyltransfer via an $\text{S}_{\text{N}}2$ -type nucleophilic substitution¹³. It is possible, therefore, that the K2 module needs the presence of at least the SAM-module to be able to accept the methyl group, a scenario highlighting the importance of cross-talk between the cluster modules during the cluster transformation process. Additionally, the fact that the amounts of SAH and 5'-dAH formed in the absence of K1 module are much reduced compared to those in the presence of K1 module further points to a coordination between all three cluster modules to maximize the efficiency of cluster transformation.

While details of the various biosynthetic events on NifB await further investigation, the current study conclusively establishes the presence of three $[\text{Fe}_4\text{S}_4]$ units on NifB and provides useful insights into the coordination and function of each module in the

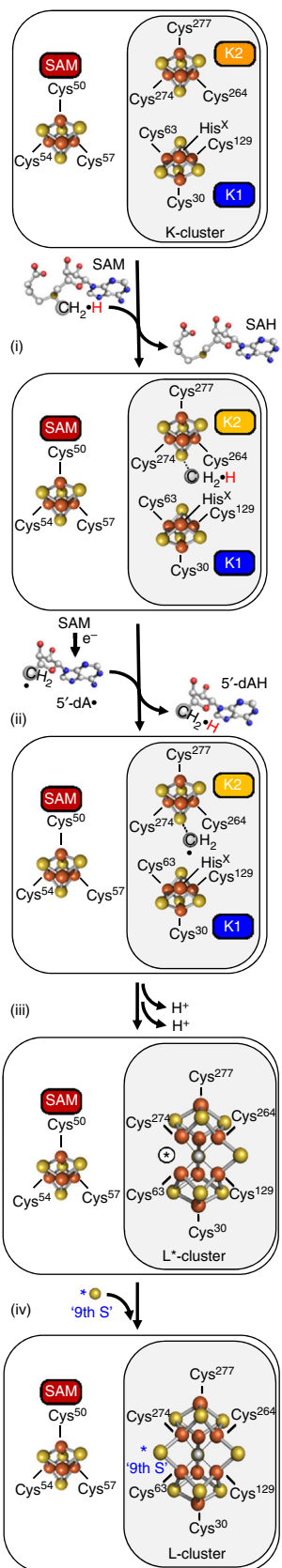


Fig. 4 Refined model of L-cluster formation on NifB. This process begins with methyltransfer from one SAM molecule to a sulfide of the K2 module via an S_N2 -type mechanism (i), and it is followed by the formation of a 5'-dA• radical via homolytic cleavage of a second SAM molecule by the SAM-module, and the subsequent hydrogen abstraction from the K2-bound methyl group by 5'-dA• (ii). The resulting, K2-bound methylene ($-\text{CH}_2\cdot$) radical then initiates the coupling/rearrangement of the K2- and K1-modules into an L*-cluster ($[\text{Fe}_8\text{S}_8\text{C}]$) that resembles the L-cluster ($[\text{Fe}_8\text{S}_9\text{C}]$) except for the absence of a belt sulfur (i.e., the 9th sulfur) (iii). Subsequently, the 9th sulfur is inserted concomitantly with further deprotonation/dehydrogenation of the carbon intermediate until an interstitial C^{4-} ion is generated in the center of a fully assembled L-cluster (iv). These events are accompanied by loss of a conserved His ligand to the K1 module and, possibly, one or more Cys ligands to both the K1- and K2-modules, to accommodate the structural rearrangement of the cluster during this process (iii, iv). This model is proposed based on data from this work and a related work²⁸. The encircled black asterisk in the scheme of L*-cluster represents the vacant site in the belt region of the cluster, which may be occupied by a cysteine thiolate or water molecule

process of K- to L-cluster transformation, taking advantage of the synthetic $[\text{Fe}_4\text{S}_4]$ -cluster-based reconstitution approach that can be applied to the functional analyses of a wide range of other FeS enzymes. The series of variants carrying different combinations of the three modules of NifB could be used to strategically uncouple the different steps in the cluster transformation process, and efforts along this line could be further combined with the identification and perturbation of the His ligand that provides the fourth N ligand to the K1 module in hopes of capturing the intermediary snapshots of this process. Advanced spectroscopic and structural investigations are underway with an ultimate goal to unveil the unique radical SAM chemistry that underscores the complex biosynthetic mechanism of the nitrogenase cofactor.

Methods

General information. Unless otherwise specified, all chemicals were purchased from Sigma-Aldrich (St. Louis, MO) and Thermo-Fisher Scientific (Waltham, MA), and all experiments were performed under an Ar atmosphere using Schlenk techniques and a glove box operating at <3 ppm O_2 .

Cell growth and protein purification. *E. coli* strains expressing His-tagged *MaNifB*^{wt} (strain YM114EE), *MaNifB*^{SAM} (strain YM163EE), *MaNifB*^{K1} (strain YM165EE), *MaNifB*^{K2} (strain YM166EE), *MaNifB*^{SAM+K1} (strain YM180EE), and *MaNifB*^{SAM+K2} (strain YM181EE) were grown in Difco LB medium containing 100 mg L^{-1} ampicillin (BD Biosciences) in a BIOFLO 415 fermenter (New Brunswick Scientific) at a temperature of 37 °C, an agitation of 200 rpm and an airflow of 10 L min^{-1} . When cell density (measured at OD_{600}) reached 0.5, 25 μM IPTG was added to the cell culture to induce protein expression at 25 °C for 16 h. Subsequently, cells were harvested by centrifugation using a Thermo-Fisher Scientific Legend XTR centrifuge, followed by purification of His-tagged *MaNifB* proteins using methods adapted from the purification of His-tagged nitrogenase proteins¹¹.

Cluster reconstitution and maturation. The as-isolated wild-type or variant *MaNifB* protein was treated with 20 mM bathophenanthroline disulfonate, an iron chelator, in a buffer containing 5 mM MgATP, 2 mM dithionite (DT; $\text{Na}_2\text{S}_2\text{O}_4$), 50 mM Tris-HCl (pH 8) and 500 mM NaCl, followed by incubation at room temperature for 1 h to remove the endogenous FeS clusters associated with the protein. Subsequently, this mixture was diluted with a buffer containing 50 mM Tris-HCl (pH 8) and loaded on a Q Sepharose column (GE Healthcare). The column was then washed with a buffer containing 2 mM DT, 50 mM Tris-HCl (pH 8) and 100 mM NaCl prior to elution of the *MaNifB* protein with a buffer containing 50 mM Tris-HCl (pH 8). Reconstitution of the wild-type or variant *MaNifB* protein with synthetic $[\text{Fe}_4\text{S}_4]$ clusters (designated $[\text{Fe}_4\text{S}_4]^{\text{Syn}}$)²⁶ was carried out by adding a dimethylformamide (DMF) solution of $[\text{Fe}_4\text{S}_4]^{\text{Syn}}$ dropwise at a molar ratio of 5:1 to the *MaNifB* protein in a buffer containing 2 mM DT, 20 mM β -mercaptoethanol, 50 mM Tris-HCl (pH 8), and 500 mM NaCl, with continuous stirring on ice. After incubation on ice for 1 h, the reaction mixture was diluted with a buffer containing 2 mM DT and 50 mM Tris-HCl (pH 8) and loaded on a Q Sepharose column. The column was then washed with a buffer containing 2 mM

DT, 50 mM Tris–HCl, and 100 mM NaCl prior to elution of the reconstituted *MaNiFB* with a buffer containing 2 mM DT, 50 mM Tris–HCl (pH 8), and 500 mM NaCl. The *MaNiFB*^{SAM}, *MaNiFB*^{K1}, *MaNiFB*^{K2}, *MaNiFB*^{SAM+K1}, and *MaNiFB*^{SAM+K2} variants were used as they were for EPR analysis, whereas *MaNiFB*^{wt} was subjected to SAM treatment using an established protocol¹⁴, during which process its K-cluster was matured into an L-cluster, prior to EPR analysis of the resultant protein species (designated *MaNiFB*^L).

Iron determination. The iron concentrations of the wild-type and variant *MaNiFB* proteins were determined by inductively coupled plasma optical emission spectroscopy (ICP-OES) using a Thermo Scientific iCAP7000. Calibration was made by using standard solutions generated from dilution of a 1 mg mL⁻¹ stock solution of elemental iron (Inorganic Ventures). Subsequently, each protein sample was mixed with 100 μ L concentrated sulfuric acid (H₂SO₄) and 100 μ L concentrated nitric acid (HNO₃), and the mixture was heated at 250 °C for 30 min. This procedure was repeated until the mixture became colorless, followed by cooling of the mixture to room temperature, and dilution of the mixture to a total volume of 10 mL with 2% HNO₃ prior to sample analysis.

SAM cleavage assays. Each SAM cleavage reaction contained 25 mM Tris–HCl (pH 8), 5% glycerol (v/v), 40 μ M *MaNiFB*, and 0.3 μ M SAM in a total volume of 0.3 mL. The reaction mixture was incubated at 25 °C for 60 min with intermittent mixing and terminated by filtration through Amicon Ultra 30,000 MWCO centrifugal filters. Subsequently, trifluoroacetic acid (TFA) was added to the reaction mixture at a concentration of 0.14%, followed by analysis of the resultant sample by a Thermo Scientific Dionex Ultimate 3000 UHPLC system, equipped with an Acclaim 120 C18 column (4.6 \times 100 mm, 5- μ m particle size). The column was equilibrated with 98% buffer A (50 mM KH₂PO₄, pH 6.6) and 2% buffer B (100% methanol) before each sample injection (100 μ L per sample) for at least 5 min. Following sample injection, a linear gradient of 2–60% buffer B was applied to the column for 20 min, followed by an isocratic flow with 60% buffer B for 8 min, and a linear gradient of 60–2% buffer B for 4 min. Throughout the run, the flow rate of buffer was kept at 0.5 mL min⁻¹, and the column was kept at 30 °C. Elution of products was monitored at a UV wavelength of 254 nm.

EPR analysis. Samples were prepared in a Vacuum Atmospheres glove box with less than 1 ppm O₂ and flash frozen in liquid nitrogen before analysis. Reduced samples contained 50 mM Tris–HCl (pH 8), 500 mM NaCl, and 2 mM DT. CW EPR spectra were recorded by an ESP 300 E_z spectrophotometer (Bruker) interfaced with an ESR-9002 liquid-helium continuous-flow cryostat (Oxford Instruments) using a microwave power of 5 mW, a gain of 5 \times 10⁴, a modulation frequency of 100 kHz, and a modulation amplitude of 5 G. Five scans of perpendicular-mode EPR were recorded at 20 K using a microwave frequency of 9.62 GHz.

For pulse EPR analysis, reaction mixtures were transferred into 4 mm (X-band)- or 2 mm (Q-band)-diameter tubes, flash frozen as above, and stored in liquid nitrogen after freezing. All pulse EPR studies were carried out at the UC Davis CalePR center, using a Bruker EleXsys E580 pulse EPR spectrometer equipped with an Oxford-CF935 liquid-helium cryostat and an ITC-503 temperature controller. Pulse data were collected using a Bruker MS5 probe (X-band) or an R.A. Isaacson-designed cylindrical TE011 resonator (Q-band)⁴⁷ adapted for pulse EPR in an Oxford Instruments CF935 cryostat. Two-pulse field swept (2PFS) EPR spectra were collected using the sequence $\pi/2$ - τ - π - τ -echo, stepping the field after each point. Three-pulse ESEEM spectra were collected using the pulse sequence $\pi/2$ - τ - $\pi/2$ - T - $\pi/2$ - τ -echo where the delay time, T , was increased by 16 ns steps. ESEEM spectra were recorded at 10 K, τ = 128–144 ns (values chosen to minimize proton modulations to the spectra), $\pi/2$ = 12 ns, and a microwave frequency of 9.3366 GHz (*MaNiFB*^{wt}, *MaNiFB*^{K1}, *MaNiFB*^{K2}) or 9.2465 GHz (*MaNiFB*^L). Spectra were collected near the g_2 value (spectra maxima) for each of the samples (*MaNiFB*^{wt}: 343 mT; *MaNiFB*^{K1}: 343 mT, and *MaNiFB*^{K2}: 344 mT, and *MaNiFB*^L: 340 mT). Hyperfine sub-level-correlation (HYSCORE) spectroscopy was performed using the pulse sequence: $\pi/2$ - τ - $\pi/2$ - T_1 - π - T_2 - $\pi/2$ - τ -echo⁴⁸. In the HYSCORE experiment, T_1 and T_2 were incremented by 20 ns steps to produce a two-dimensional spectrum. HYSCORE spectra were recorded at 10 K, τ = 128–132 ns, and $\pi/2$ = 12 ns. Spectral processing and simulations were performed using the EasySpin 4.0 toolbox in Matlab R2017b⁴⁹.

All spin quantification was carried out using the program SpinCount⁵⁰. Variable power EPR spectra were collected for *MaNiFB*^{SAM}, *MaNiFB*^{K1} and *MaNiFB*^{K2} at 20 K to determine the extent of saturation. All *MaNiFB* samples were found to have a linear response to the microwave power across all values tested. Samples of Cu(II) EDTA between 0.1 mM and 0.5 mM were used as standards for the $S = 1/2$ signals observed for *MaNiFB* variants, at microwave powers between 0.5 and 1 mW. The slope of each spectrum was baseline corrected using the program tools in SpinCount. The double integral was measured across the $S = 1/2$ signal for each spectrum. The integrations were compared between the Cu(II)EDTA standard and the *MaNiFB* samples to determine the spin concentration.

Acid quench experiments. A published method was adapted for the *MaNiFB*-dependent production of methanethiol^{13,51}. The procedure involved removal of

excess DT from *MaNiFB* via gel filtration with Sephadex G-25 fine resin that was equilibrated with a buffer containing 25 mM Tris–HCl (pH 8). Subsequently, 40 nmol of *MaNiFB* was mixed with 400 nmol SAM in a total volume of 100 μ L in a sealed 300- μ L glass vial, incubated for 30 min at 25 °C, and quenched by 25 μ L of 1 M HCl. The acid-quenched sample was then incubated at 60 °C for 15 min to release the volatile methanethiol into the headspace, followed by equilibration of the sample to room temperature for 10 min, and injection of the entire headspace by a gas-tight syringe onto a Restek Rxi-1ms column (30 m, 0.32 mm ID, 4 μ m df) for analysis by GC–MS (Thermo-Fisher Scientific Trace 1300 GC connected to a Thermo-Fisher Scientific ISQ QD single quadrupole mass spectrometry). During each GC–MS run, the GC inlet and oven temperatures were kept at 30 °C, and the mass spectrometry transfer line and ion source were kept at 250 °C. Using SIM conditions in electron ionization mode, methanethiol was detected at an m/z ratio of 47.

Data availability. The authors declare that all data supporting the findings of this study are available within the article and the Supplementary Information and from the corresponding authors upon reasonable request.

Received: 19 March 2018 Accepted: 21 June 2018

Published online: 19 July 2018

References

- Burgess, B. K. & Lowe, D. J. Mechanism of molybdenum nitrogenase. *Chem. Rev.* **96**, 2983–3012 (1996).
- Rees, D. C. et al. Structural basis of biological nitrogen fixation. *Philos. Trans. A Math. Phys. Eng. Sci.* **363**, 971–984 (2005).
- Hoffman, B. M., Lukyanov, D., Yang, Z. Y., Dean, D. R. & Seefeldt, L. C. Mechanism of nitrogen fixation by nitrogenase: the next stage. *Chem. Rev.* **114**, 4041–4062 (2014).
- Lee, C. C., Hu, Y. & Ribbe, M. W. Vanadium nitrogenase reduces CO. *Science* **329**, 642 (2010).
- Hu, Y., Lee, C. C. & Ribbe, M. W. Extending the carbon chain: hydrocarbon formation catalyzed by vanadium/molybdenum nitrogenases. *Science* **333**, 753–755 (2011).
- Einsle, O. et al. Nitrogenase MoFe-protein at 1.16 Å resolution: a central ligand in the FeMo-cofactor. *Science* **297**, 1696–1700 (2002).
- Spatzal, T. et al. Evidence for interstitial carbon in nitrogenase FeMo cofactor. *Science* **334**, 940 (2011).
- Lancaster, K. M. et al. X-ray emission spectroscopy evidences a central carbon in the nitrogenase iron-molybdenum cofactor. *Science* **334**, 974–977 (2011).
- Sickerman, N. S., Ribbe, M. W. & Hu, Y. Nitrogenase cofactor assembly: an elemental inventory. *Acc. Chem. Res.* **50**, 2834–2841 (2017).
- Hu, Y. & Ribbe, M. W. Maturation of nitrogenase cofactor—the role of a class E radical SAM methyltransferase NifB. *Curr. Opin. Chem. Biol.* **31**, 188–194 (2016).
- Wiig, J. A., Hu, Y. & Ribbe, M. W. NifEN-B complex of *Azotobacter vinelandii* is fully functional in nitrogenase FeMo cofactor assembly. *Proc. Natl Acad. Sci. USA* **108**, 8623–8627 (2011).
- Wiig, J. A., Hu, Y., Lee, C. C. & Ribbe, M. W. Radical SAM-dependent carbon insertion into the nitrogenase M-cluster. *Science* **337**, 1672–1675 (2012).
- Wiig, J. A., Hu, Y. & Ribbe, M. W. Refining the pathway of carbide insertion into the nitrogenase M-cluster. *Nat. Commun.* **6**, 8034 (2015).
- Fay, A. W., Wiig, J. A., Lee, C. C. & Hu, Y. Identification and characterization of functional homologs of nitrogenase cofactor biosynthesis protein NifB from methanogens. *Proc. Natl Acad. Sci. USA* **112**, 14829–14833 (2015).
- Hu, Y. et al. FeMo cofactor maturation on NifEN. *Proc. Natl Acad. Sci. USA* **103**, 17119–17124 (2006).
- Yoshizawa, J. M. et al. Optimization of FeMoco maturation on NifEN. *J. Am. Chem. Soc.* **131**, 9321–9325 (2009).
- Kaiser, J. T., Hu, Y., Wiig, J. A., Rees, D. C. & Ribbe, M. W. Structure of precursor-bound NifEN: a nitrogenase FeMo cofactor maturase/insertase. *Science* **331**, 91–94 (2011).
- Fay, A. W. et al. Spectroscopic characterization of the isolated iron-molybdenum cofactor (FeMoco) precursor from the protein NifEN. *Angew Chem. Int. Ed.* **50**, 7787–7790 (2011).
- Hu, Y. et al. Nitrogenase Fe protein: a molybdate/homocitrate insertase. *Proc. Natl Acad. Sci. USA* **103**, 17125–17130 (2006).
- Schmid, B. et al. Structure of a cofactor-deficient nitrogenase MoFe protein. *Science* **296**, 352–356 (2002).
- Frey, P. A., Hegeman, A. D. & Ruzicka, F. J. The radical SAM superfamily. *Crit. Rev. Biochem. Mol. Biol.* **43**, 63–88 (2008).
- Broderick, J. B., Duffus, B. R., Duschene, K. S. & Shepard, E. M. Radical S-adenosylmethionine enzymes. *Chem. Rev.* **114**, 4229–4317 (2014).

23. Shah, V. K. et al. In vitro synthesis of the iron-molybdenum cofactor of nitrogenase. Purification and characterization of NifB cofactor, the product of NifB protein. *J. Biol. Chem.* **269**, 1154–1158 (1994).
24. Allen, R. M. et al. Incorporation of iron and sulfur from NifB cofactor into the iron-molybdenum cofactor of dinitrogenase. *J. Biol. Chem.* **270**, 26890–26896 (1995).
25. George, S. J. et al. Extended X-ray absorption fine structure and nuclear resonance vibrational spectroscopy reveal that NifB-co, a FeMo-co precursor, comprises a 6Fe core with an interstitial light atom. *J. Am. Chem. Soc.* **130**, 5673–5680 (2008).
26. Guo, Y. et al. The nitrogenase FeMo-cofactor precursor formed by NifB protein: a diamagnetic cluster containing eight iron atoms. *Angew. Chem. Int. Ed.* **55**, 12764 (2016).
27. Wilcoxon, J. et al. Electron paramagnetic resonance characterization of three iron-sulfur clusters present in the nitrogenase cofactor maturase NifB from *Methanocaldococcus infernus*. *J. Am. Chem. Soc.* **138**, 7468–7471 (2016).
28. Tanifuji, K. et al. Tracing the '9th sulfur' of the nitrogenase cofactor via a semi-synthetic approach. *Nat. Chem.* **10**, 568–572 (2018).
29. Taylor, A. M. et al. Reduction of the [2Fe–2S] cluster accompanies formation of the intermediate 9-mercaptodethiobiotin in *Escherichia coli* biotin synthase. *Biochemistry* **50**, 7953–7963 (2011).
30. Dicus, M. M. et al. Binding of histidine in the (Cys)₃(His)₁-coordinated [2Fe–2S] cluster of human mitoNEET. *J. Am. Chem. Soc.* **132**, 2037–2049 (2010).
31. Gurbel, R. J. et al. Electron-nuclear double resonance spectroscopy of ¹⁵N-enriched phthalate dioxygenase from *Pseudomonas cepacia* proves that two histidines are coordinated to the [2Fe–2S] Rieske-type clusters. *Biochemistry* **28**, 4861–4871 (1989).
32. Britt, R. D. et al. Electron spin echo envelope modulation spectroscopy supports the suggested coordination of two histidine ligands to the Rieske iron-sulfur centers of the cytochrome b₆f complex on spinach and the cytochrome bc₁ complexes of *Rhodospirillum rubrum*, *Rhodobacter sphaeroides* R-26, and bovine heart mitochondria. *Biochemistry* **30**, 1892–1901 (1991).
33. Shergill, J. K. et al. ESEEM and ENDOR studies of the Rieske iron-sulphur protein in bovine heart mitochondrial membranes. *Biochim. Biophys. Acta* **1185**, 35–42 (1994).
34. Riedel, A. et al. EPR, Electron spin echo envelope modulation, and electron nuclear double resonance studies of the 2Fe2S centers of the 2-halobenzoate 1,2-dioxygenase from *Burkholderia (Pseudomonas) cepacia* 2CBS. *J. Biol. Chem.* **270**, 30869–30873 (1995).
35. Shergill, J. K. et al. Coordination of the Rieske-type [2Fe–2S] cluster of the terminal iron-sulfur protein of *Pseudomonas putida* benzene 1,2-dioxygenase, studied by one- and two-dimensional electron spin-echo envelope modulation spectroscopy. *Biochemistry* **34**, 16533–16542 (1995).
36. Dikanov, S. A. et al. Orientationally-selected two-dimensional ESEEM spectroscopy of the Rieske-type iron-sulfur cluster in 2,4,5-trichlorophenoxyacetate monooxygenase from *Burkholderia cepacia* AC1100. *J. Am. Chem. Soc.* **118**, 8408–8416 (1996).
37. Gurbel, R. J. et al. Active site structure of Rieske-type proteins: electron nuclear double resonance studies of isotopically labeled phthalate dioxygenase from *Pseudomonas cepacia* and Rieske protein from *Rhodobacter capsulatus* and molecular modeling studies of a Rieske center. *Biochemistry* **35**, 7834–7845 (1996).
38. Dikanov, S. A. et al. A comparative, two-dimensional ¹⁴N ESEEM characterization of reduced [2Fe–2S] clusters in hyperthermophilic archaeal high- and low-potential Rieske-type proteins. *J. Biol. Inorg. Chem.* **9**, 753–767 (2004).
39. Lees, N. S. et al. ENDOR spectroscopy shows that guanine N1 binds to [4Fe–4S] cluster II of the S-adenosylmethionine-dependent enzyme MoeA: mechanistic implications. *J. Am. Chem. Soc.* **131**, 9184–9185 (2009).
40. Dikanov, S. A. & Tsvetkov, Y. D. *Electron Spin Echo Envelope Modulation (ESEEM) Spectroscopy* (CRC Press Inc., Boca Raton, FL, 1992).
41. Scholes, C. P. et al. Electron nuclear double resonance (ENDOR) from heme and histidine nitrogens in single crystals of aquometmyoglobin. *J. Am. Chem. Soc.* **104**, 2724–2735 (1982).
42. Boal, A. K. et al. Structural basis for methyl transfer by a radical SAM enzyme. *Science* **332**, 1089–1092 (2011).
43. Grove, T. L., Radle, M. I., Krebs, C. & Booker, S. J. Cfr and RlmN contain a single [4Fe–4S] cluster, which directs two distinct reactivities for S-adenosylmethionine: methyl transfer by S_N2 displacement and radical generation. *J. Am. Chem. Soc.* **133**, 19586–19589 (2011).
44. Schwalm, E. L., Grove, T. L., Booker, S. J. & Boal, A. K. Crystallographic capture of a radical S-adenosylmethionine enzyme in the act of modifying tRNA. *Science* **352**, 309–312 (2016).
45. Karmi, O. et al. The unique fold and lability of the [2Fe–2S] clusters of NEET proteins mediate their key functions in health and disease. *J. Biol. Inorg. Chem.* **23**, 599–612 (2018).
46. Tamir, S. et al. Structure–function analysis of NEET proteins uncovers their role as key regulators of iron and ROS homeostasis in health and disease. *Biochim. Biophys. Acta* **1853**, 1294–1315 (2015).
47. Flores, M. et al. Probing hydrogen bonding to quinone anion radicals by ¹H and ²H ENDOR spectroscopy at 35 GHz. *J. Chem. Phys.* **294**, 401–413 (2006).
48. Schweiger, A. & Jeschke, G. *Principles of Pulse Electron Paramagnetic Resonance* (Oxford University Press, Oxford, UK, 2001).
49. Stoll, S. & Schweiger, A. EasySpin, a comprehensive software package for spectral simulation and analysis in EPR. *J. Magn. Reson.* **178**, 42–55 (2006).
50. Petasis, D. T. & Hendrich, M. P. Quantitative interpretation of multifrequency multimode EPR spectra of metal containing proteins, enzymes, and biomimetic complexes. *Methods Enzymol.* **563**, 171–208 (2015).
51. Lanz, N. D. et al. RlmN and AtsB as models for the overproduction and characterization of radical SAM proteins. *Methods Enzymol.* **516**, 125–152 (2012).

Acknowledgements

We thank Prof. Markus W. Ribbe (UCI) for helpful discussions. This work was supported by NIH-NIGMS grant GM67626 (to Prof. Markus W. Ribbe and Y.H.) and NIH-NIHGMS grant 1R35GM126961-01 (to R.D.B.).

Author contributions

L.A.R., J.W., C.C.L., M.T.S. and K.T. performed experiments and analyzed data; J.W., R.D.B. and Y.H. designed experiments, analyzed data, and wrote the manuscript.

Additional information

Supplementary Information accompanies this paper at <https://doi.org/10.1038/s41467-018-05272-8>.

Competing interests: The authors declare no competing interests.

Reprints and permission information is available online at <http://npg.nature.com/reprintsandpermissions/>

Publisher's note: Springer Nature remains neutral with regard to jurisdictional claims in published maps and institutional affiliations.



Open Access This article is licensed under a Creative Commons Attribution 4.0 International License, which permits use, sharing, adaptation, distribution and reproduction in any medium or format, as long as you give appropriate credit to the original author(s) and the source, provide a link to the Creative Commons license, and indicate if changes were made. The images or other third party material in this article are included in the article's Creative Commons license, unless indicated otherwise in a credit line to the material. If material is not included in the article's Creative Commons license and your intended use is not permitted by statutory regulation or exceeds the permitted use, you will need to obtain permission directly from the copyright holder. To view a copy of this license, visit <http://creativecommons.org/licenses/by/4.0/>.

© The Author(s) 2018